

# Direct fabrication of graphitic carbon nitride-wrapped titanate nanotube arrays toward photoelectrochemical water oxidation in neutral medium

Tho Truong Nguyen\*, Hong-Huy Tran<sup>\*\*,\*\*\*</sup>, Thi Minh Cao\*, and Viet Van Pham<sup>\*\*,\*\*\*,†</sup>

\*HUTECH University, 475A Dien Bien Phu Street, Binh Thanh District, Ho Chi Minh City, 700000, Vietnam

\*\*Faculty of Materials Science and Technology, University of Science, VNU-HCM,  
227 Nguyen Van Cu Street, District 5, Ho Chi Minh City, 700000, Vietnam

\*\*\*Vietnam National University Ho Chi Minh City, Thu Duc City, Ho Chi Minh City, 700000, Vietnam

(Received 22 December 2021 • Revised 10 March 2022 • Accepted 2 April 2022)

**Abstract**—Realizing a long-term, high-performance, and affordable photocatalytic setting for water splitting processes remains challenging despite the tremendous promise. We present a direct fabrication of graphitic carbon nitride-wrapped titanate nanotube array ( $\text{gC}_3\text{N}_4$ -wrapped TNA) heterojunction photoelectrodes via a chemical vapor deposition-like process that leverages the pyrolysis and sublimation of melamine at 500 °C. The  $\text{gC}_3\text{N}_4$ -wrapped TNA heterojunction photoelectrodes show a 16 times enhancement of current density and photo-response than bare TNAs. Such a remarkable enhancement comes from the effective charge separation of the  $\text{gC}_3\text{N}_4$ /TNA interfaces, consequently accelerating water splitting to generate oxygen under visible light. In addition, our  $\text{gC}_3\text{N}_4$ -wrapped TNA photoelectrodes are developed under a neutral condition that significantly increases their widespread use for practical devices.

Keywords:  $\text{TiO}_2$  Nanotube Arrays, Graphitic Carbon Nitride, Water Splitting, Water Oxidation, Pyrolysis Deposition

## INTRODUCTION

Photoelectrochemical (PEC) water splitting to generate hydrogen and oxygen plays a central role in realizing our ambitious 2030 Sustainable Development Goals of energy efficiency and sustainable energy [1-5]. The origin of this remarkable progress comes from its sustainability, recyclability, low cost, and high energy conversion efficiency. However, it remains challenging to have a practically efficient energy conversion device.

Developing stable and high-performance photocatalytic materials for water splitting processes has been one of the most active research areas in this modern era. The astonishing performance generally comes from noble or rare materials [6-10]. However, such noble materials are rare and costly, undoubtedly hindering their widespread adoption in large-scale applications. Thus, several strategies have been implemented against the dependence of these noble and rare materials by using such materials in the form of single atoms or ultrathin layers [11-21]. Despite the possible reduction in the use of noble materials, these approaches inevitably consume an incredible total of noble materials, inadvertently affecting the goals for a sustainable nature.

Titanate nanotube arrays (TNAs) represent a unique class of photoelectrode materials for water splitting because of their highly oriented charge transport paths, significant specific surface areas, photo and chemical stability, slow charge recombination, ease of fabrication, and low cost [22-29]. Therefore, extensive approaches have been proposed to use TNAs as a photoelectrode for efficient water

splitting. Such strategies include metal loading [30,31], doping [23, 32], bandgap engineering [33,34], narrow bandgap semiconductor coupling [35,36], and surface engineering [37,38].

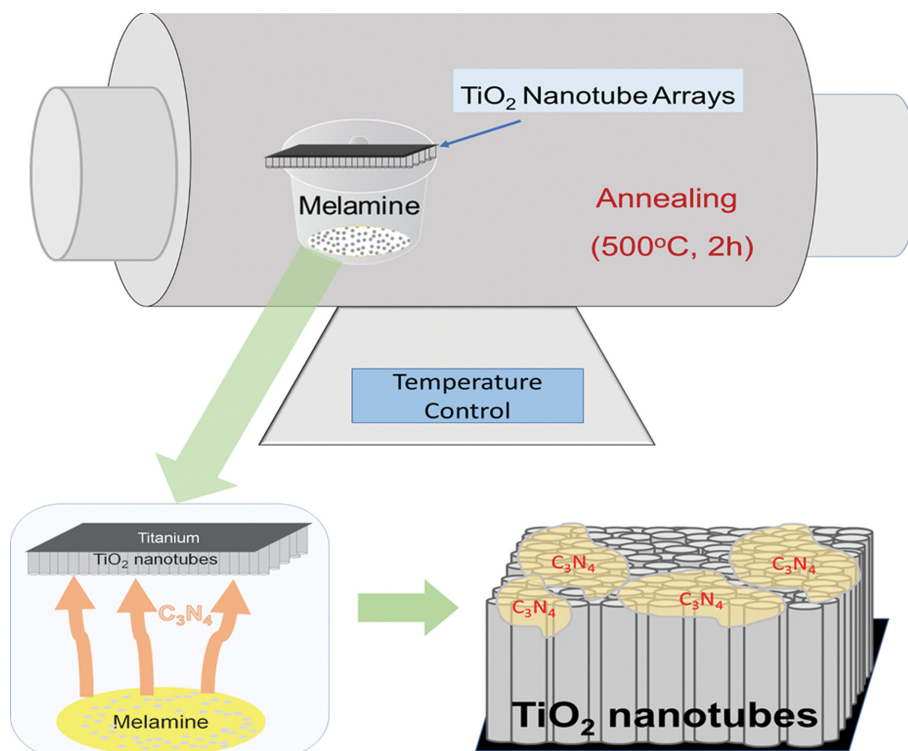
Notably, coupling with metal-free graphitic carbon nitride ( $\text{gC}_3\text{N}_4$ ) holds great potential for constructing practically efficient photoelectrodes. The origin for making such a combination to leap comes from the tremendous inherent advantage of  $\text{gC}_3\text{N}_4$ , showing an excellent visible light response, non-toxicity, low cost, and ease of manufacture [39-44]. Specifically,  $\text{gC}_3\text{N}_4$ /TNA heterojunction materials significantly improve PEC water splitting performance [45-47]. This remarkable combination originates from the proper bandgap configuration between  $\text{TiO}_2$  and  $\text{gC}_3\text{N}_4$ . However, the documented performance of these  $\text{gC}_3\text{N}_4$ / $\text{TiO}_2$  heterojunctions is strictly constrained because of the low specific surface area and poor electrical conductivity of  $\text{gC}_3\text{N}_4$  [48,49]. Additionally, the conventional approaches for fabricating these structures are complicated, laborious, poorly reproducible, and time-consuming, which hinders their potential for scalable manufacturing. In addition, reported studies mainly focus on alkaline media, which do not meet the practical conditions [50-53].

In this work, we directly fabricated  $\text{gC}_3\text{N}_4$ -wrapped TNA heterojunction photoelectrodes via a chemical vapor deposition-like process. We induced deposition of  $\text{gC}_3\text{N}_4$  on the surface of TNAs through the melamine sublimation at 500 °C. The as-obtained  $\text{gC}_3\text{N}_4$ -wrapped TNA photoelectrodes show an excellent photo-response ability because of their enhanced charge density and effectively prolonged charge recombination, indicating an improvement in water splitting under visible light. Also, our  $\text{gC}_3\text{N}_4$ -wrapped TNA photoelectrodes are developed under neutral conditions, which has practical significance in the environmental and economic advantages.

<sup>†</sup>To whom correspondence should be addressed.

E-mail: pvviet@hcmus.edu.vn

Copyright by The Korean Institute of Chemical Engineers.



Scheme 1. A schematic illustration of the deposition of  $gC_3N_4$  onto TNA photoelectrodes. The objects are not drawn to scale for clarity.

## EXPERIMENTAL

### 1. Chemicals and Materials

Titanium (Ti) foils with a thickness of 0.125 mm were provided by Alfa Aesar (USA). Sodium hydroxide (NaOH, 99%, Fisher chemical, USA), hydrochloric acid (HCl, 36.5%, Fisher chemical, USA), acetone ( $C_3H_6O$ , Fisher BioReagents, USA), and absolute ethanol ( $C_2H_5OH$ , Fisher BioReagents, USA) were used to clean the surface of Ti foils. Ethylene glycol ( $C_2H_6O_2$ , 99%, Fisher Chemical, USA), deionized water (DI) (MilliQ,  $18\text{ M}\Omega\text{ cm}^{-1}$ ), and ammonium fluoride ( $NH_4F$ , 96%, Fisher Chemical, USA). Melamine ( $C_3H_6N_6$ ),  $K_2Cr_2O_7$ , and KI chemicals were provided by Acros Organics (USA) with a purity of 99%.

### 2. Preparation of Materials

Preparation of TNAs: Highly ordered TNAs were prepared via a two-step anodization oxidation process [54]. Briefly, the Ti foils were cut into  $1\text{ cm}\times 2\text{ cm}$  pieces and polished by sandpaper (Kovax P1000), followed by immersing in 10% HCl and 12 M NaOH solutions, respectively, to remove surface contaminants. Next, these Ti pieces were sonicated in acetone, ethanol, and DI water, respectively, followed by a drying step at  $60^\circ\text{C}$  for 30 min. The electrolyte solution was prepared by dissolving 0.25 g  $NH_4F$  in 4.5 mL DI water. Then, 40.5 mL of ethylene glycol was added with continuous stirring for 15 min. Anodic oxidation was performed in a two-electrode electrochemical cell in a Teflon-lined steel reactor. The Ti foil and Pt wire were used as anode and cathode, respectively. In the first anodic oxidation cycle, the Ti foil was applied a DC voltage of 30 V for 2 h, resulting in  $TiO_2$  and partly developed TNAs on the surface of Ti pieces. Next, this surface was treated with son-

ication in a DI water medium for 10 min, removing the unnecessary oxide layer and leaving nucleation sites for the later growth of TNAs. The surface was then ready for the second anodic oxidation cycle at the same voltage for 30 min. Commonly, the sample was rinsed with DI water after the anodization process, followed by drying and annealing steps at  $60^\circ\text{C}$  and  $500^\circ\text{C}$  for 2 h, respectively.

Preparation of  $gC_3N_4$ -wrapped TNA photoelectrodes:  $gC_3N_4$ -wrapped TNAs were fabricated through a chemical vapor deposition-like process based on the pyrolysis of melamine, as illustrated in Scheme 1. Briefly, 0.3 g of melamine was placed in a crucible together with a TNA photoelectrode, covering the surface of melamine (Scheme 1). A hole with a diameter of 6 mm was drilled on the lid of the crucible where the TNA was positioned, followed by an annealing process at  $500^\circ\text{C}$  for 2 h.

### 3. Characterizations of Materials

Fourier transform infrared spectrophotometer (FTIR) analysis was studied in the range of  $400\text{--}4,000\text{ cm}^{-1}$  using a JASCO V4700 to investigate molecular vibrations of the materials. The material layer was collected from the Ti substrate, then mixed with KBr at a 1/300 (sample/KBr) ratio. The sample was prepared by molding it into a pellet shape with a diameter of 1 cm. X-ray diffraction (XRD) patterns were used to determine the materials' phase composition and crystal structure using a Bruker D8 X-ray diffractometer with the Cu K radiation ( $\lambda=0.154064\text{ nm}$ ) and the scanning rate of  $0.02^\circ\text{ min}^{-1}$  in the  $2\theta$  range of  $10^\circ\text{--}80^\circ$ . The surface morphology of the materials was observed by scanning electron microscope (SEM) images, captured on a Hitachi SEM Hitachi S4800 at an accelerating voltage of 10 kV. The X-ray photoelectron spectra (XPS) were conducted on a PHI Hybrid Quantera photoelectron spectrome-

ter, using a monochromate 450 W Al K $\alpha$  source as the exciting source.

#### 4. Photoelectrochemical Water Oxidation Properties of Materials

The PEC water splitting of the materials was studied in a neutral medium, using a three-electrodes PEC cell on a Biologic SP-200 (France). The as-prepared materials were used as a working electrode, Pt wire was used as a counter electrode, and Ag/AgCl 3 M NaCl were reference electrodes. A 1 M Na<sub>2</sub>SO<sub>4</sub> (pH 7.4) solution was used as the electrolyte solution. The light source was provided by a solar simulator lamp, ABET Instruments, using a Xenon lamp with a power of 150 W. A UV filter was used to leave only the visible light passing. The potential V vs. Ag/AgCl was converted into a V vs. RHE relation using the Nernst equation (Eq. (1)).

$$E_{RHE} = E_{Ag/AgCl} + E_{0(Ag/AgCl)} + 0.059 \times \text{pH} \quad (1)$$

where  $E_{0(Ag/AgCl)} = 0.210$  V at 25 °C, a pH value of 7.4 was recorded for the electrolyte solution.

The linear sweep voltammogram (LSV) analysis of the as-prepared materials was recorded by observing the current density vs. the applied linear potential in the range of -1 to 1 V vs. Ag/AgCl in a neutral medium. The photo-response ability of the materials was captured by applying a potential voltage of 0 V vs. Ag/AgCl under repetitive on-off illumination conditions.

Mott-Schottky plots were obtained at a frequency of 1 kHz, amplitude of 10 mV, in the potential range of -1 to 1 V vs Ag/AgCl. The flat band potential is generally obtained from capacitance versus voltage (CV) measurements. The observed capacitance values are subsequently incorporated into the following Mott-Schottky equation to evaluate the flat band potential, according to Eq. (2) [55]:

$$\frac{1}{C^2} = \frac{2}{\epsilon \epsilon_0 A^2 q N_d} \left( V - V_f - \frac{k_B T}{q} \right) \quad (2)$$

where, C is the semiconductor/metal or semiconductor/electrolyte junction capacitance,  $\epsilon$  is the dielectric constant of semiconductor, V is the applied potential,  $V_f$  is flat band potential,  $N_d$  is doping density, A is the area of the depletion region/space charge region,  $k_B$  is Boltzmann's constant, T is the absolute temperature at which the measurement is performed. The above equation plot yields a straight line from which the flat band potential  $V_f$  of a given semiconductor can be extracted.

## RESULTS AND DISCUSSION

### 1. Material Characterization

Fig. 1 shows the diffraction peaks of TNAs at  $2\theta = 25^\circ$ ,  $47.16^\circ$ , and  $70.05^\circ$ , characterized by the (101), (200), and (220) lattice planes of anatase phase TiO<sub>2</sub>, respectively (JCPDS No. 21-1272). In addition, the diffraction peak recorded at  $2\theta = 37.27^\circ$  represents the (100) lattice plane of the titanium substrate. The XRD pattern of gC<sub>3</sub>N<sub>4</sub> presents two characteristic peaks at  $2\theta = 13.1^\circ$  and  $27.9^\circ$ , corresponding to the (100) and (002) planes of gC<sub>3</sub>N<sub>4</sub>, respectively (JCPDS 87-1526). Also, these two peaks are attributed to the in-plane structure of tri-s-triazine units and the interlayer stacking of conjugated aromatic groups in gC<sub>3</sub>N<sub>4</sub>. For the gC<sub>3</sub>N<sub>4</sub>-wrapped TNA sample, the presence of, at the same time, typical diffraction peaks of gC<sub>3</sub>N<sub>4</sub> and TNAs is observed, indicating the success in making gC<sub>3</sub>N<sub>4</sub>/TNA

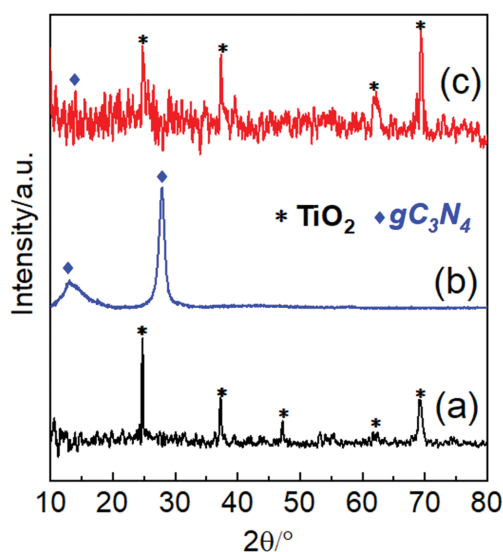


Fig. 1. XRD patterns of TNA (a), gC<sub>3</sub>N<sub>4</sub> (b), and gC<sub>3</sub>N<sub>4</sub>-wrapped TNA samples (c).

composites. The diffraction peak intensity of gC<sub>3</sub>N<sub>4</sub> in the gC<sub>3</sub>N<sub>4</sub>-wrapped TNA sample is relatively low, likely due to the low concentration of gC<sub>3</sub>N<sub>4</sub> introduction in the heterojunction. Such a combination also induces a change in the crystal orientation of the composite where the (220) lattice plane is the most oriented. The difference in crystallinity of TiO<sub>2</sub> materials after combining with other materials to form heterojunctions was previously observed because the formation of this heterojunction structure relates to the competitive growth between component materials [56,57].

The compositional information and chemical bonds of TNA, gC<sub>3</sub>N<sub>4</sub>, and gC<sub>3</sub>N<sub>4</sub>-wrapped TNA samples are characterized by FTIR spectroscopy. In Fig. 2(a), the typical peaks in the region from 450 cm<sup>-1</sup> to 750 cm<sup>-1</sup> for TNAs are attributed to Ti-O-Ti and Ti-O stretching vibration modes in anatase TiO<sub>2</sub> crystals. The formation

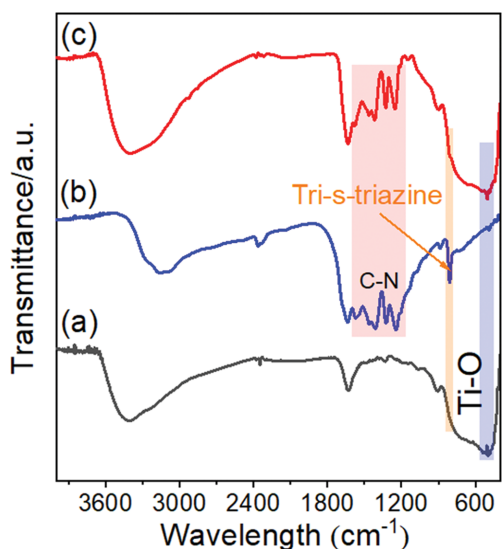


Fig. 2. FTIR spectra of TNAs (a), gC<sub>3</sub>N<sub>4</sub> (b), and gC<sub>3</sub>N<sub>4</sub>-wrapped TNAs (c).

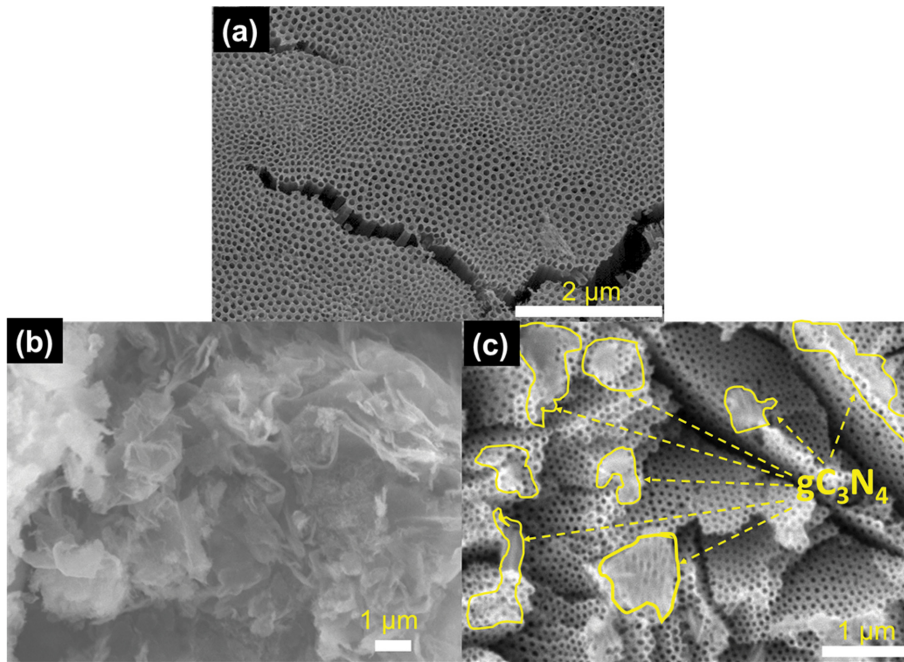


Fig. 3. SEM images of TNAs (a), gC<sub>3</sub>N<sub>4</sub> (b), and gC<sub>3</sub>N<sub>4</sub>-wrapped TNAs (c).

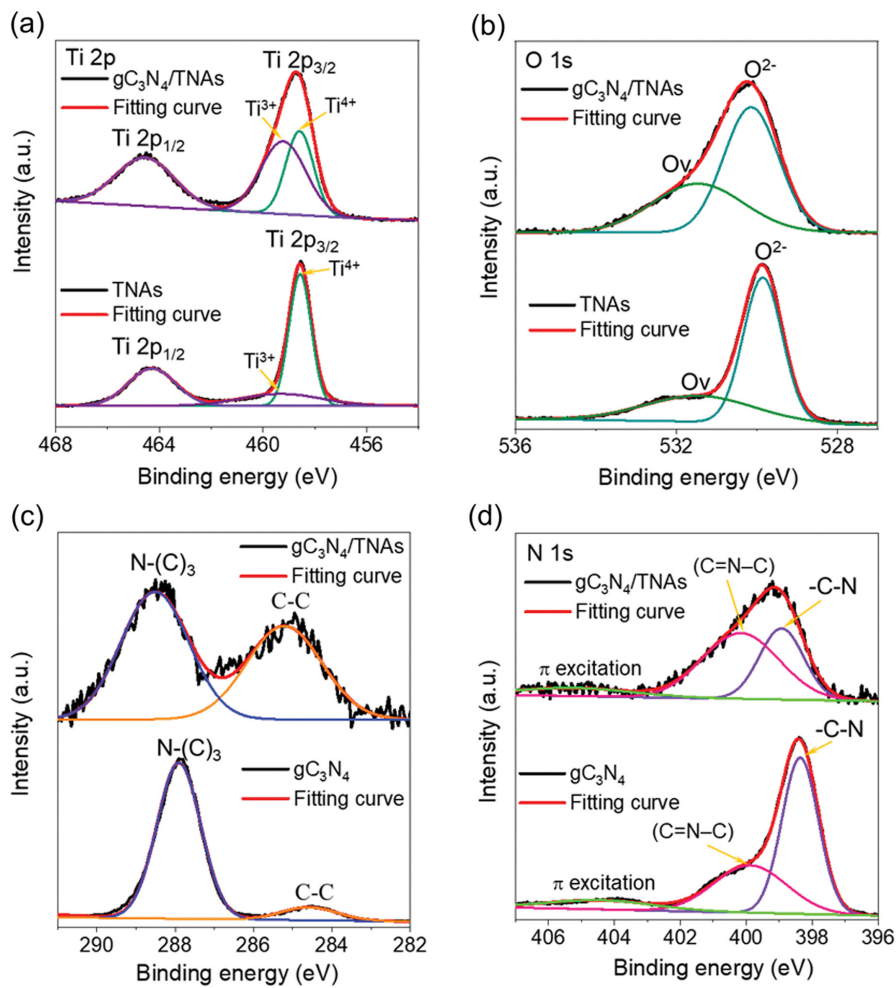


Fig. 4. High resolution XPS of Ti 2p (a), O 1s (b), C 1s (c), and N 1s (d).

of the  $gC_3N_4$  material is characterized through C-N oscillation states ranging from 1,200 to 1,640  $cm^{-1}$  (Fig. 2(b)). Besides, a sharp peak at 809  $cm^{-1}$  is attributed to the characteristic breathing mode of tri-s-triazine units. Furthermore, the FTIR result of the  $gC_3N_4$ -wrapped TNA in Fig. 2(c) has given the most distinctive peaks of  $gC_3N_4$  and  $TiO_2$ . The coexistence of  $TiO_2$  and  $gC_3N_4$  in  $gC_3N_4$ -wrapped TNA heterojunction is thus confirmed.

The morphology of the materials is captured via SEM images, as shown in Fig. 3. After the two steps of the anodic oxidation process, the surface of the Ti foil is densely covered by hollow nanostructures with uniformity in diameter size ( $\sim 75$  nm), as shown in Fig. 3(a). Specifically, the nanotubes arrange closer to each other, eliminating the cavities between nanotubes. Fig. 3(b) shows the morphology of the  $gC_3N_4$  after an annealing process at 500  $^{\circ}C$ , generally having a sheet-like structure. Upon being combined by our chemical vapor deposition-like process, the surface of the TNAs is wrapped by  $gC_3N_4$  sheets, as shown in Fig. 3(c). In addition, this result shows a significant change of the morphology of the TNAs upon being combined with  $gC_3N_4$ .

The high-resolution XPS (HR-XPS) spectra are recorded to accurately analyze the surface chemical composition and valence state of the elements in the as-obtained materials. Fig. 4(a) shows the HR-XPS of the Ti 2p orbital; three deconvoluted peaks at 462.40, 457.42, and 456.68 eV are observed for the TNAs sample, indicating Ti 2p<sub>3/2</sub>, Ti<sup>3+</sup>, and Ti 2p<sub>1/2</sub> states, respectively [58]. This result indicates that the oxidation state of Ti ions is not wholly Ti<sup>4+</sup> since there is a small amount of Ti<sup>3+</sup> states. The HR-XPS Ti 2p profile of the  $gC_3N_4$ -wrapped TNAs sample shows a slight shift toward higher binding energies, suggesting a possible migration of electrons from the  $gC_3N_4$  to TNAs [59]. Total area percentages of fitting spectra for Ti 2p in TNAs and  $gC_3N_4$ /TNAs are shown in Table 1. Briefly, the total area percentage of Ti 2p<sub>3/2</sub> peak in TNAs is 51.68%, while  $gC_3N_4$ /TNAs is only 27.44%. In the reverse direction, the total area percentage of Ti<sup>3+</sup> in TNAs is 17.0%, but considerably increased to 38.8% in the  $gC_3N_4$ /TNAs. However, the density of Ti 2p<sub>1/2</sub> remains unchanged. The total area percentage of Ti 2p<sub>1/2</sub> in TNAs is 31.32% and is 33.74% in  $gC_3N_4$ /TNAs. These results indicate the migration of electrons from  $gC_3N_4$  to TNAs, causing a additional reduc-

**Table 1. Percentage of the total area for Ti 2p, Ti<sup>3+</sup> in TNAs and  $gC_3N_4$ /TNAs**

Sample	Peak area by integrating data (%)		
	Ti 2p <sub>3/2</sub>	Ti 2p <sub>1/2</sub>	Ti <sup>3+</sup>
TNAs	51.68	31.32	17.0
$gC_3N_4$ /TNAs	27.44	33.74	38.82

tion of Ti<sup>4+</sup> to Ti<sup>3+</sup>.

O 1s peaks are recorded at 529.8 and 531.5 eV for the TNAs sample (Fig. 4(b)), which are typically assigned to the lattice oxygen (O<sup>2-</sup>) and oxygen vacancies (O<sub>v</sub>) in TiO<sub>2</sub> materials [60]. However, the peak of O<sup>2-</sup> shifts to higher binding energy, located at 530.1 eV, suggesting an interfacial interaction between TNA and  $gC_3N_4$ . In the HR-XPS C 1s profiles of the obtained materials, two typical peaks are observed at 284.6 and 287.9 eV, presenting the C-C and N-(C)<sub>3</sub> bonds, respectively (Fig. 4(c)) [61]. In addition, the N 1s peaks of sp<sup>2</sup>-hybridized aromatic N(C=N-C) (398.4 eV) and C-N-H groups (399.9 eV), as shown in Fig. 4(d). However, these peaks show an apparent shift toward higher binding energies. Precisely, the shifted peaks are located at 285.2 eV for C-C, 288.5 eV for N-(C)<sub>3</sub>, 398.9 eV for N(C=N-C), and 400.2 eV for C-N-H. These observations strongly support the hypothesis on the migration of electrons from  $gC_3N_4$  to the TNAs, leading to decreased electron density. Thus, the HR-XPS results indicate the strong interaction between TNAs and  $gC_3N_4$  at the interface. This evidence has clearly shown the formation of the heterostructure  $gC_3N_4$ -wrapped TNAs. The results present a remarkable agreement between the characterization results, clearly indicating the successful fabrication of the  $gC_3N_4$ -wrapped TNA nanocomposites via our direct chemical vapor deposition-like process.

## 2. Photoelectrochemical Water Oxidation Ability in the Neutral Medium of $gC_3N_4$ -wrapped TNAs

The LSV in the dark and under the illumination of the materials is explored for the oxygen evolution reaction (OER) studies with a three-electrode electrochemical cell in 1 M Na<sub>2</sub>SO<sub>4</sub> solution at a pH of 7.4 (Fig. 5(a)). The difference of TNAs with the thermal treat-

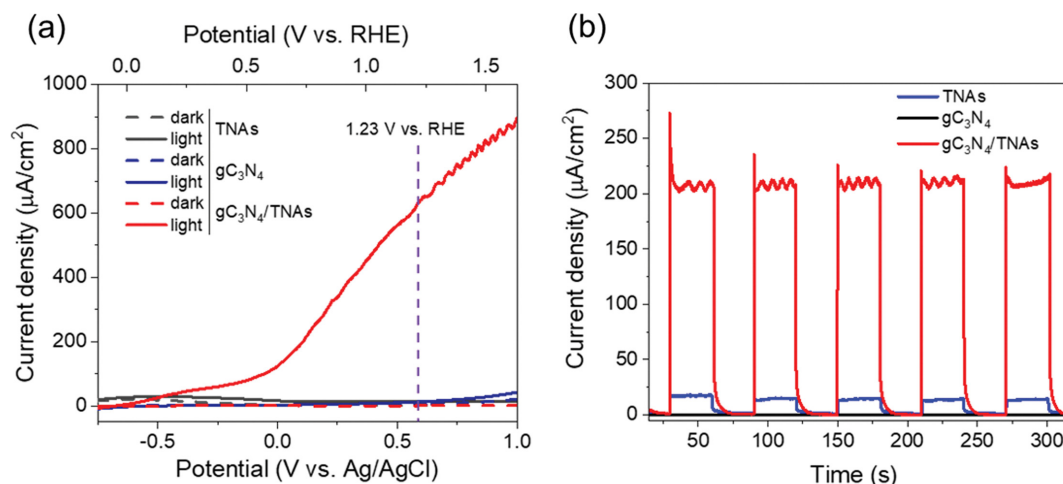


**Fig. 5. LSV of materials (a), and photocurrent density of materials at 0.63 V vs. RHE (b) in 1M Na<sub>2</sub>SO<sub>4</sub> electrolyte (pH 7.4).**

**Table 2. A comparison of photocurrent on this work with other publications**

Electrode materials	Method	Morphology of materials	Applied potential	Electrolyte	pH medium	Current density ( $\mu\text{A}/\text{cm}^2$ )	Ref.
$\text{g-C}_3\text{N}_4/\text{TiO}_2$	Thermal decomposition	Nanosheets/ Nanotube arrays	0 V vs. SCE	0.5 M $\text{Na}_2\text{SO}_4$	Not provided	1.79	[65]
$\text{Pt}/\text{g-C}_3\text{N}_4/\text{TNTs}$	Chemical vapor deposition	Nanosheets/ Nanotube arrays	0.75 V vs. Ag/AgCl	0.1 M $\text{Na}_2\text{SO}_4$	Not provided	10	[65]
$\text{g-C}_3\text{N}_4/\text{TNAs}$	Electrochemical	Nanosheets/ Nanotube arrays	0 V vs. SCE	0.5 M $\text{Na}_2\text{SO}_4$	Not provided	4	[66]
$\text{g-C}_3\text{N}_4/\text{TiO}_2$	Electrodeposition	Nanosheets/ Nanotube arrays	1 V vs. Ag/AgCl	1 M $\text{Na}_2\text{SO}_4$	Not provided	140	[67]
$\text{g-C}_3\text{N}_4/\text{Pt}/\text{TiO}_2$	Chemical adsorption and calcination	Nanosheets/ Spheres	-	1 M $\text{Na}_2\text{SO}_4$	Not provided	0.08	[68]
$\text{g-C}_3\text{N}_4/\text{TiO}_2$	Microwave-heating technique	Nanoparticles/ Nanocorns	-	0.5 M $\text{Na}_2\text{SO}_4$	Not provided	6.8	[69]
$\text{g-C}_3\text{N}_4/\text{TNAs}$	Thermal decomposition	Nanosheets/ Nanotube arrays	0.63 V vs. RHE	1 M $\text{Na}_2\text{SO}_4$	7.4	206	This study

ment at 500 °C and TNAs without the thermal treatment has also been indicated as in Fig. S1. In detail, the photoresponse ability of TNAs without thermal treatment has a current density of 2.87  $\mu\text{A}/\text{cm}^2$ , while that of TNAs 500 °C is around 17.51  $\mu\text{A}/\text{cm}^2$  in the first cycle of irradiation. Therefore, we conducted investigations of TNAs 500 °C sample in the experimental works. As in Fig. 5(a), the current density of the materials under dark conditions is negligible. However, under the illumination, all the materials present the ability to generate current. Specifically, under the illumination and the applied potential scanned from -0.37 V vs. RHE to 1.63 V vs. RHE, the PEC ability of the  $\text{gC}_3\text{N}_4$ -wrapped TNAs presents the highest value. The onset potential of TNAs is obtained at -0.22 vs. RHE, and the current density at the highest applied potential value is about 14  $\mu\text{A}/\text{cm}^2$ . The onset potential of  $\text{gC}_3\text{N}_4$  is about -0.07 V vs. RHE, and the current density at the highest applied potential value is about 43.3  $\mu\text{A}/\text{cm}^2$ . A superior OER activity is recorded over the  $\text{gC}_3\text{N}_4$ -wrapped TNAs sample. In detail, the onset potential of  $\text{gC}_3\text{N}_4$ -wrapped TNAs is obtained around -0.05 V vs. RHE. The current density slope is enormously increased from 0.6 V vs. RHE and linear to the applied potential. At 1.63 V vs. RHE, the current density of  $\text{gC}_3\text{N}_4$ -wrapped TNAs can reach around 895.1  $\mu\text{A}/\text{cm}^2$ , 64 and 21 folds higher than that of the TNAs and  $\text{gC}_3\text{N}_4$  samples, respectively (Fig. 5(a)). This result means that the charge recombination is hindered by accelerating the electron's transfer. In addition, at the applied potential of 1.23 V vs. RHE, which is known as  $E_0$  for splitting  $\text{O}_2$  from  $\text{H}_2\text{O}$  (at pH 0), the  $\text{gC}_3\text{N}_4$ -wrapped TNAs sample expresses a current density of 635.1  $\mu\text{A}/\text{cm}^2$ , indicating a strong performance in PEC in comparison with the single-component samples. By these results, the increase of carrier concentration after creating the interface between  $\text{gC}_3\text{N}_4$  and TNAs is achieved.

The photo-response ability of the materials under visible light is shown in Fig. 5(b). The discontinuity cycle of the illumination is kept at 30 s. The interaction of the materials to the visible light is obtained through the difference of current density under on-off operations. As shown in Fig. 5(b), the current density of the TNAs

sample under irradiation is about 4.3  $\mu\text{A}/\text{cm}^2$ . In contrast, that of  $\text{gC}_3\text{N}_4$  is very low, just about 1  $\mu\text{A}/\text{cm}^2$ . However, the formation of  $\text{gC}_3\text{N}_4$ -wrapped TNAs heterojunctions strongly enhances the photocurrent density. The current density of the  $\text{gC}_3\text{N}_4$ -wrapped TNAs is obtained at about 274.1  $\mu\text{A}/\text{cm}^2$  in the early stage of illumination and kept stable at around 206  $\mu\text{A}/\text{cm}^2$  even after five cycles. This result is still 48-fold higher than that of the TNAs sample. This result again demonstrates the success in increasing the carrier concentration and amending the recombination of  $e^- - h^+$  in the heterojunction. Such an observation is already evidenced from the XPS results, leading to an increase in the current density and likely enhancing the PEC performance. A comparison is made to demonstrate the improvement in PEC performance of the  $\text{gC}_3\text{N}_4$ -wrapped TNAs heterostructure in our work, as shown in Table 2. In addition, the effect of sacrificial agents (s.a.) to the PEC activities of materials was investigated to determine the role of carriers in the catalysis process. In detail, we used 0.1 mM of  $\text{K}_2\text{Cr}_2\text{O}_7$  and KI as scavenger agents of photogenerated  $e^-$  and  $h^+$ , respectively, to add the  $\text{Na}_2\text{SO}_4$  1 M electrolyte solution in the photocatalytic reaction [62,63]. The results of the effect of the s.a. are indicated in Fig. S2(a). Therein, the LSV of  $\text{gC}_3\text{N}_4/\text{TNAs}$  with the presence of KI in the electrolyte displays a low current density. At 1.23 V vs. RHE, the current density under irradiation is only around 41.5  $\mu\text{A}/\text{cm}^2$ . This result indicates the importance of  $h^+$  in the OER process of PEC water splitting. Otherwise, LSV of  $\text{gC}_3\text{N}_4/\text{TNAs}$  with the presence of  $\text{K}_2\text{Cr}_2\text{O}_7$  in the electrolyte shows a strongly enhanced current density in comparison with that of normal electrolyte. Fig. S2(b) shows the current density at an applied potential of 1.23 V vs. RHE under irradiation can reach to 975.4  $\mu\text{A}/\text{cm}^2$ . The improvement in current density is explained due to the presence of scavenger agent, which reduces the recombination of  $e^- - h^+$  pairs. In addition, maximum photocurrents are also affected by the presence of the  $\text{K}_2\text{Cr}_2\text{O}_7$  as a strong  $h^+$  donor agent, leading to enhance OER process in PEC water splitting [64].

The Mott-Schottky plot is considered an effective method to ana-

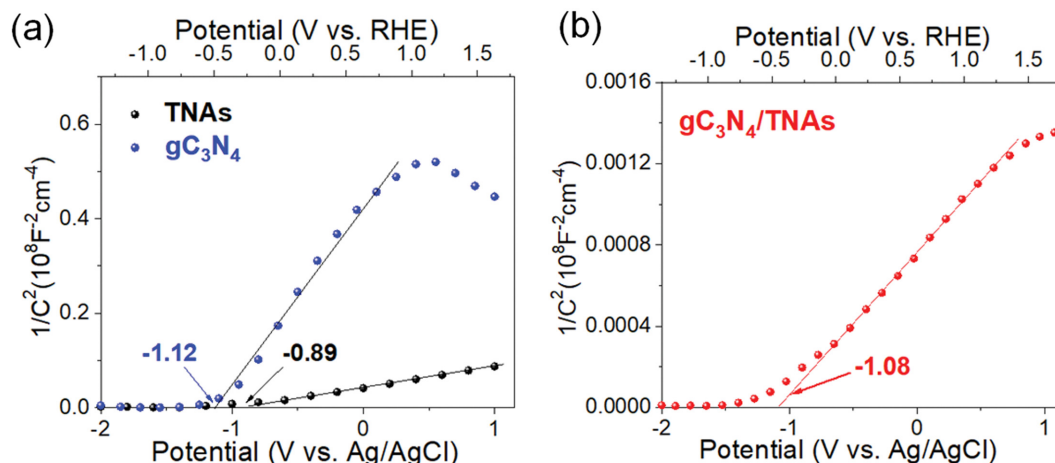


Fig. 6. Mott-Schottky plots of TNAs,  $gC_3N_4$  (a) and  $gC_3N_4$ -wrapped TNA (b).

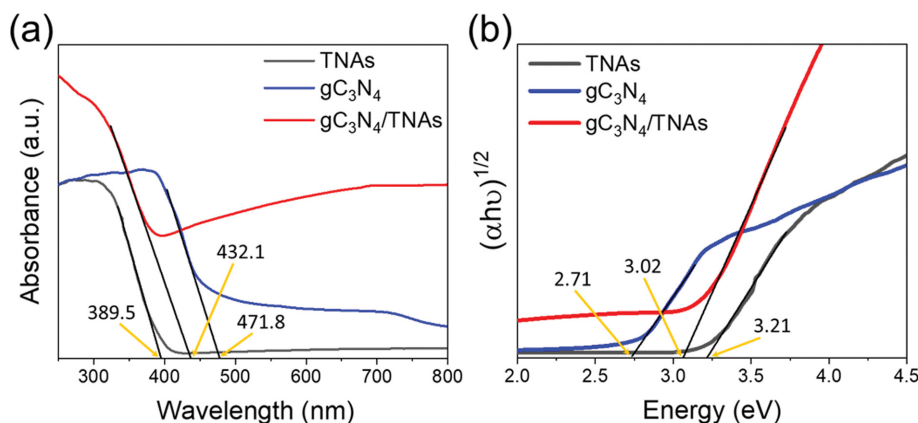


Fig. 7. DRS spectra (a) and Tauc plots (b) of materials.

lyze the electrochemical properties of materials, the behavior of the carriers, states of the semiconductor materials. As shown in Fig. 6, the Mott-Schottky plots of all materials in this contribution have been obtained through positive slopes. This indicates that all samples pose n-type semiconductor properties. From the Mott-Schottky results in Fig. 6 and according to Eq. (2), the CB levels of the materials are obtained at  $-0.31$  V vs. RHE,  $-0.47$  V vs. RHE, and  $-0.45$  V vs. RHE for TNAs,  $gC_3N_4$  and  $gC_3N_4$ -wrapped TNAs, respectively. As shown in Fig. 6(a), the CB of  $gC_3N_4$  is much higher than that of TNAs. This could promote the  $e^-$  migration from  $gC_3N_4$  to the TNAs. As shown in Fig. 6(b), the CB of  $gC_3N_4$ -wrapped TNAs is shifted to a higher level than TNAs. Besides, the intensity of  $1/C^2$  slope of  $gC_3N_4$ -wrapped TNAs is much lower than that of TNAs and  $gC_3N_4$ , indicating a higher charge storage capacity. A smaller slope suggests that the  $gC_3N_4$ -wrapped TNAs sample has a higher carrier density and much faster carrier transfer, agreeing with the PEC results. This evidence has proven the richness of  $e^-$  after creating the heterojunction.

To evaluate the interaction of the materials with radiation, DRS spectra and Tauc plots of the materials were obtained and shown in Fig. 7. As can be seen in Fig. 7(a), the TNAs sample is only activated in the UV range, which is demonstrated through an absorption edge at 389.5 nm in the DRS result. Besides, the DRS spectrum

of  $gC_3N_4$  shows an absorption edge.

In contrast, the  $gC_3N_4$  material shows an absorption edge at 471.8 nm, which allows  $gC_3N_4$  to perform photocatalytic reactions in the visible light region. Moreover, for this reason,  $gC_3N_4$  is considered as a potential candidate for modification of pristine  $TiO_2$  material to form a heterostructure that could enhance optical interaction. This phenomenon is indicated by the DRS spectra of  $gC_3N_4$ /TNAs heterostructure. The absorption band edge is shifted to 432.1 nm compared to pristine TNAs. Furthermore, the absorbance of  $gC_3N_4$ /TNAs in the range after 432.1 nm is also higher than that of TNAs and  $gC_3N_4$ , which allows this heterostructure to enhance photoelectrochemical water splitting signals. To evaluate the optical bandgap energy for the indirect bandgap semiconductor, such as  $TiO_2$  and  $gC_3N_4$ , Tauc plots of the materials are extrapolated through the Eq. (3) and shown in Fig. 7(b) [70].

$$\alpha hv = A(hv - E_g)^{1/2} \quad (3)$$

The bandgap of TNAs,  $gC_3N_4$ , and  $gC_3N_4$ /TNAs is calculated at about 3.21 eV, 2.71 eV, and 3.02 eV, respectively. As can be seen, the bandgap of  $gC_3N_4$ /TNAs is strongly reduced compared to that of TNAs. These results have demonstrated the efficiency in the modification of TNAs by  $gC_3N_4$ .

We have successfully obtained a  $gC_3N_4$ -wrapped TNA photoelec-

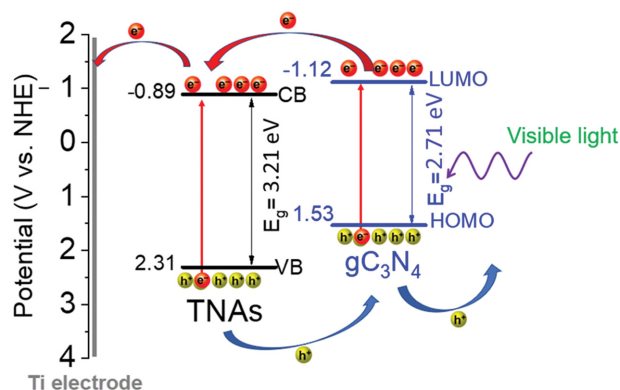


Fig. 8. Schematic illustration of charge transfer pathway in  $gC_3N_4$ -wrapped TNAs heterojunction for water oxidation activity.

trode based on the presented results, showing excellent water oxidation in a neutral medium under visible light. The enhanced water oxidation originates from efficient charge separation because of the formed interface between  $gC_3N_4$  and TNA through the chemical vapor deposition-like process. Based on the Mott-Schottky plots and Tauc plots, a proposition of possible mechanism for the photocatalytic water oxidation of the  $gC_3N_4$ -wrapped TNAs has been shown in Fig. 8. Because the conduction band (CB) position of the  $gC_3N_4$  is more negative than that of the  $TiO_2$  [41,71], an internal local electric field is formed. This phenomenon induces the migration of photogenerated electrons from the CB of  $gC_3N_4$  to the TNAs and the Ti electrode, which contributes significantly in the PEC activity of  $gC_3N_4$ -wrapped TNAs (as in Fig. S2). Spontaneously, the holes in the valence band (VB) of the TNAs transfer to the VB of the  $gC_3N_4$ , which readily oxidize the surrounding water and leads to efficient charge separation and effective water splitting.

## CONCLUSION

We have described the direct fabrication of  $gC_3N_4$ -wrapped TNA heterojunctions via a chemical vapor deposition-like process by taking advantage of the pyrolysis of melamine to form  $gC_3N_4$  that then is quickly deposited on the surface of TNAs. The  $gC_3N_4$ -wrapped TNA heterojunctions show excellent water splitting at a neutral medium. Precisely, such a  $gC_3N_4$ -wrapped TNA heterojunction has a current density of  $224 \mu A/cm^2$  at 0.6 V vs. Ag/AgCl, which is 16 times higher than that of the TNAs. This enhancement originates from forming an interface between  $gC_3N_4$  and TNAs, accelerating the photo-response of this heterojunction under visible light.

## ACKNOWLEDGEMENTS

The authors thank Ms. Pham Thi Kieu Oanh for the initial experimental setting of this study. This research is funded by the HUTECH University under grant number 63/HĐ-ĐKC (2019/02/19/CNC).

## NOTES

The authors declare no competing financial interest.

## SUPPORTING INFORMATION

Additional information as noted in the text. This information is available via the Internet at <http://www.springer.com/chemistry/journal/11814>.

## REFERENCES

- G. Dolf, B. Francisco and S. Deger, *Nat. Mater.*, **15**, 117 (2016).
- S. Chu, Y. Cui and N. Liu, *Nat. Mater.*, **16**, 16 (2016).
- S. Chu and A. Majumdar, *Nature*, **488**, 294 (2012).
- M. G. Walter, E. L. Warren, J. R. McKone, S. W. Boettcher, Q. Mi, E. A. Santori and N. S. Lewis, *Chem. Rev.*, **110**, 6446 (2010).
- C. Jiang, S. J. A. Moniz, A. Wang, T. Zhang and J. Tang, *Chem. Soc. Rev.*, **46**, 4645 (2017).
- B. Liu, C. H. Kuo, J. Chen, Z. Luo, S. Thanneeru, W. Li, W. Song, S. Biswas, S. L. Suib and J. He, *Angew. Chem. Int. Ed.*, **54**, 9061 (2015).
- R. R. Rao, M. J. Kolb, N. B. Halck, A. F. Pedersen, A. Mehta, H. You, K. A. Stoerzinger, Z. Feng, H. A. Hansen, H. Zhou, L. Giordano, J. Rossmeisl, T. Vegge, I. Chorkendorff, I. E. L. Stephens and Y. Shao-Horn, *Energy Environ. Sci.*, **10**, 2626 (2017).
- P. Jiang, J. Chen, C. Wang, K. Yang, S. Gong, S. Liu, Z. Lin, M. Li, G. Xia, Y. Yang, J. Su and Q. Chen, *Adv. Mater.*, **30** (2018).
- L. Fu, F. Yang, G. Cheng and W. Luo, *Nanoscale*, **10**, 1892 (2018).
- E. Khorashadizade, S. Mohajernia, S. Hejazi, H. Mehdipour, N. Naseri, O. Moradlou, A. Z. Moshfegh and P. Schmuki, *J. Phys. Chem. C*, **125**, 6116 (2021).
- X. Zhou, I. Hwang, O. Tomanec, D. Fehn, A. Mazare, R. Zboril, K. Meyer and P. Schmuki, *Adv. Funct. Mater.*, **31**, 2102843 (2021).
- L. Zhuang, L. Ge, Y. Yang, M. Li, Y. Jia, X. Yao and Z. Zhu, *Adv. Mater.*, **29** (2017).
- X. Li, W. Bi, L. Zhang, S. Tao, W. Chu, Q. Zhang, Y. Luo, C. Wu and Y. Xie, *Adv. Mater.*, **28**, 2427 (2016).
- C. Ling, L. Shi, Y. Ouyang, X. C. Zeng and J. Wang, *Nano Lett.*, **17**, 5133 (2017).
- C. Zhu, Q. Shi, S. Feng, D. Du and Y. Lin, *ACS Energy Lett.*, **3**, 1713 (2018).
- J. Zhang, C. Liu and B. Zhang, *Small Methods*, **3**, 1800481 (2019).
- W. H. Lai, L. F. Zhang, W. B. Hua, S. Indris, Z. C. Yan, Z. Hu, B. Zhang, Y. Liu, L. Wang, M. Liu, R. Liu, Y. X. Wang, J. Z. Wang, Z. Hu, H. K. Liu, S. L. Chou and S. X. Dou, *Angew. Chem. Int. Ed.*, **58**, 11868 (2019).
- X. Zheng, J. Tang, A. Gallo, J. A. Garrido Torres, X. Yu, C. J. Athanitis, E. M. Been, P. Ercius, H. Mao, S. C. Fakra, C. Song, R. C. Davis, J. A. Reimer, J. Vinson, M. Bajdich and Y. Cui, *Proc. Natl. Acad. Sci. USA*, **118** (2021).
- X. Li, S. Zhao, X. Duan, H. Zhang, S.-z. Yang, P. Zhang, S. P. Jiang, S. Liu, H. Sun and S. Wang, *Appl. Catal. B*, **283**, 119660 (2021).
- A. Alarawi, V. Ramalingam and J.-H. He, *Mater. Today Energy*, **11**, 1 (2019).
- Q. Wang, Z. Zhang, C. Cai, M. Wang, Z. L. Zhao, M. Li, X. Huang, S. Han, H. Zhou, Z. Feng, L. Li, J. Li, H. Xu, J. S. Francisco and M. Gu, *J. Am. Chem. Soc.*, **143**, 13605 (2021).
- F. Fu, Z. Wu, G. Cha and P. Schmuki, *Chem. Commun.*, **57**, 7120 (2021).
- J. H. Park, S. Kim and A. J. Bard, *Nano Lett.*, **6**, 28 (2006).

24. I. S. Cho, J. Choi, K. Zhang, S. J. Kim, M. J. Jeong, L. Cai, T. Park, X. Zheng and J. H. Park, *Nano Lett.*, **15**, 5709 (2015).
25. Z. Zhang, M. F. Hossain and T. Takahashi, *Int. J. Hydrogen Energy*, **35**, 8528 (2010).
26. S. Liang, J. He, Z. Sun, Q. Liu, Y. Jiang, H. Cheng, B. He, Z. Xie and S. Wei, *J. Phys. Chem. C*, **116**, 9049 (2012).
27. X. Cheng, Y. Zhang and Y. Bi, *Nano Energy*, **57**, 542 (2019).
28. Q.-q. Meng, J.-g. Wang, Q. Xie, H.-q. Dong and X.-n. Li, *Catal. Today*, **165**, 145 (2011).
29. J. Gong, Y. Lai and C. Lin, *Electrochim. Acta*, **55**, 4776 (2010).
30. X. Fan, J. Fan, X. Hu, E. Liu, L. Kang, C. Tang, Y. Ma, H. Wu and Y. Li, *Ceram. Int.*, **40**, 15907 (2014).
31. Y. Lai, J. Gong and C. Lin, *Int. J. Hydrogen Energy*, **37**, 6438 (2012).
32. S. W. Shin, J. Y. Lee, K.-S. Ahn, S. H. Kang and J. H. Kim, *J. Phys. Chem. C*, **119**, 13375 (2015).
33. H. Cui, W. Zhao, C. Yang, H. Yin, T. Lin, Y. Shan, Y. Xie, H. Gu and F. Huang, *J. Mater. Chem. A*, **2**, 8612 (2014).
34. Z. Li, H. Bian, X. Xiao, J. Shen, C. Zhao, J. Lu and Y. Y. Li, *ACS Appl. Nano Mater.*, **2**, 7372 (2019).
35. Y. Yin, Z. Jin and F. Hou, *Nanotechnology*, **18**, 495608 (2007).
36. J. Lin, Y. Liu, Y. Liu, C. Huang, W. Liu, X. Mi, D. Fan, F. Fan, H. Lu and X. Chen, *ChemSusChem*, **12**, 961 (2019).
37. Q. Gui, Z. Xu, H. Zhang, C. Cheng, X. Zhu, M. Yin, Y. Song, L. Lu, X. Chen and D. Li, *ACS Appl. Mater. Interfaces*, **6**, 17053 (2014).
38. J. Luo, Y. Ma, H. Wang and J. Chen, *Electrochim. Acta*, **167**, 119 (2015).
39. X. Lu, Z. Liu, J. Li, J. Zhang and Z. Guo, *Appl. Catal. B*, **209**, 657 (2017).
40. B. Rhimi, C. Wang and D. W. Bahnemann, *J. Phys. Energy*, **2**, 042003 (2020).
41. P. V. Viet, N. H. Phuong, T. H. Huy, B. D. Phat, L. V. Hai, P. M. Thuan, S. J. You and C. M. Thi, *J. Sci.-Adv. Mater. Dev.*, **17**, 2101070 (2021).
42. Q. Zhu, Z. Xu, B. Qiu, M. Xing and J. Zhang, *Small*, **6**, 551 (2021).
43. L. Wang, Y. Tong, J. Feng, J. Hou, J. Li, X. Hou and J. Liang, *SM&T*, **19**, 00089 (2019).
44. Y. Hou, Z. Wen, S. Cui, X. Feng and J. Chen, *Nano Lett.*, **16**, 2268 (2016).
45. L. Xiao, T. Liu, M. Zhang, Q. Li and J. Yang, *ACS Sustain. Chem. Eng.*, **7**, 2483 (2018).
46. W. Kong, X. Zhang, B. Chang, Y. Zhou, S. Zhang, G. He, B. Yang and J. Li, *Electrochim. Acta*, **282**, 767 (2018).
47. C. Liu, F. Wang, J. Zhang, K. Wang, Y. Qiu, Q. Liang and Z. Chen, *Nanomicro. Lett.*, **10**, 37 (2018).
48. C. Pan, J. Xu, Y. Wang, D. Li and Y. Zhu, *Adv. Funct. Mater.*, **22**, 1518 (2012).
49. W. Ma, D. Han, M. Zhou, H. Sun, L. Wang, X. Dong and L. Niu, *Chem. Sci.*, **5**, 3946 (2014).
50. M. Wang, S. Dipazir, P. Lu, Y. Wang, M. Yuan, S. Li and G. Zhang, *J. Colloid Interface Sci.*, **532**, 774 (2018).
51. B. Zhang, C. Xiao, S. Xie, J. Liang, X. Chen and Y. Tang, *Chem. Mater.*, **28**, 6934 (2016).
52. D. Liu, Q. Lu, Y. Luo, X. Sun and A. M. Asiri, *Nanoscale*, **7**, 15126 (2015).
53. A. Sivanantham, P. Ganesan and S. Shanmugam, *Adv. Funct. Mater.*, **26**, 4661 (2016).
54. N. T. Tho, C. M. Thi, L. V. Hieu and P. V. Viet, *J. Aust. Ceram. Soc.*, **56**, 849 (2019).
55. O. Almora, C. Aranda, E. Mas-Marzá and G. Garcia-Belmonte, *Appl. Phys. Lett.*, **109**, 173903 (2016).
56. P. V. Viet, T. H. Huy, N. X. Sang, C. M. Thi and L. V. Hieu, *J. Mater. Sci.*, **53**, 3364 (2017).
57. P. V. Viet, B. D. Phat, T. H. Huy, C. M. Thi, N. T. Khoa, K. Y. Soo and L. V. Hieu, *RSC Adv.*, **8**, 12420 (2018).
58. S. Singh, V. Sharma and K. Sachdev, *J. Mater. Sci.*, **52**, 11580 (2017).
59. D. Jiang, X. Sun, H. Zhang, K. Wang, L. Shi and F. Du, *Appl. Phys. A*, **126** (2020).
60. A. Ghobadi, T. G. Ulusoy, R. Garifullin, M. O. Guler and A. K. Okyay, *Sci. Rep.*, **6**, 30587 (2016).
61. W. Zhang, L. Zhou and H. Deng, *J. Mol. Catal. A Chem.*, **423**, 270 (2016).
62. L. P. P. Ha, T. H. T. Vinh, N. T. B. Thuy, C. M. Thi and P. V. Viet, *J. Environ. Chem. Eng.*, **9**, 105103 (2021).
63. T. K. Thao, N. Q. Thang, L. P. P. Ha, L. V. Hai, T. V. Man, C. M. Thi and P. V. Viet, *Chemosphere*, **268**, 129291 (2021).
64. F. E. Bedoya Lora, A. Hankin and G. H. Kelsall, *J. Mater. Chem. A*, **5**, 22683 (2017).
65. M. Sun, Y. Fang, Y. Kong, S. Sun, Z. Yu and A. Umar, *J. Chem. Soc., Dalton Trans.*, **45**, 12702 (2016).
66. D. Zhou, Z. Chen, Q. Yang, C. Shen, G. Tang, S. Zhao, J. Zhang, D. Chen, Q. Wei and X. Dong, *ChemCatChem*, **8**, 3064 (2016).
67. B. Pandey, S. Rani and S. C. Roy, *J. Alloys Compd.*, **846**, 155881 (2020).
68. B. Chai, T. Peng, J. Mao, K. Li and L. Zan, *Phys. Chem. Chem. Phys.*, **14**, 16745 (2012).
69. C. Pan, J. Jia, X. Hu, J. Fan and E. Liu, *Appl. Surf. Sci.*, **430**, 283 (2018).
70. B. Rezaei, N. Irannejad and A. A. Ensafi, *Renew. Energy*, **123**, 281 (2018).
71. T. H. Huy, D. P. Bui, F. Kang, Y. F. Wang, S. H. Liu, C. M. Thi, S. J. You, G. M. Chang and P. V. Viet, *Chemosphere*, **215**, 323 (2019).

## Supporting Information

### Direct fabrication of graphitic carbon nitride-wrapped titanate nanotube arrays toward photoelectrochemical water oxidation in neutral medium

Tho Truong Nguyen\*, Hong-Huy Tran\*\*,\*\*\*, Thi Minh Cao\*, and Viet Van Pham\*\*,\*\*\*,†

\*HUTECH University, 475A Dien Bien Phu Street, Binh Thanh District, Ho Chi Minh City, 700000, Vietnam

\*\*Faculty of Materials Science and Technology, University of Science, VNU-HCM,  
227 Nguyen Van Cu Street, District 5, Ho Chi Minh City, 700000, Vietnam

\*\*\*Vietnam National University - Ho Chi Minh City, Thu Duc District, Ho Chi Minh City, 700000, Vietnam

(Received 22 December 2021 • Revised 10 March 2022 • Accepted 2 April 2022)

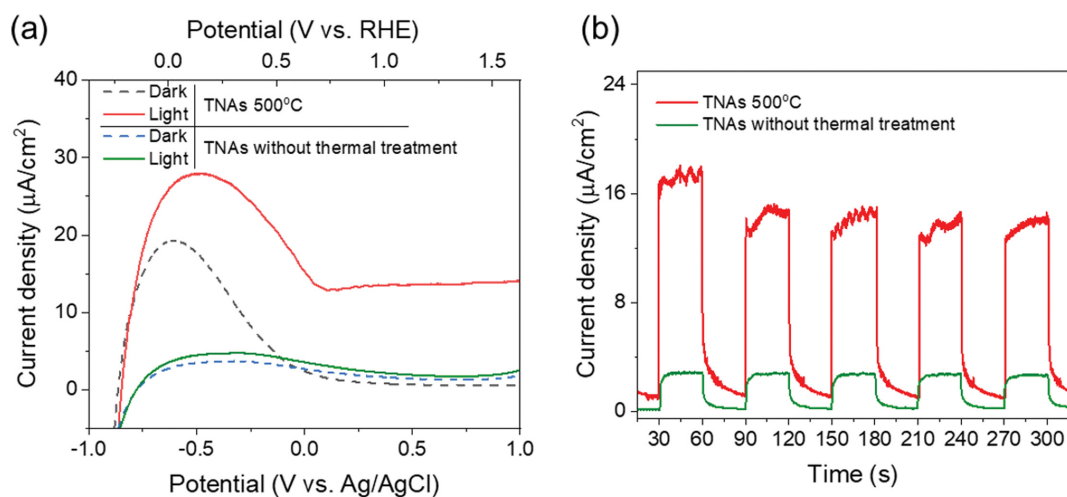


Fig. S1. LSV (a) and photoresponse ability (b) TNAs treated at 500°C and TNAs without thermal treatment.

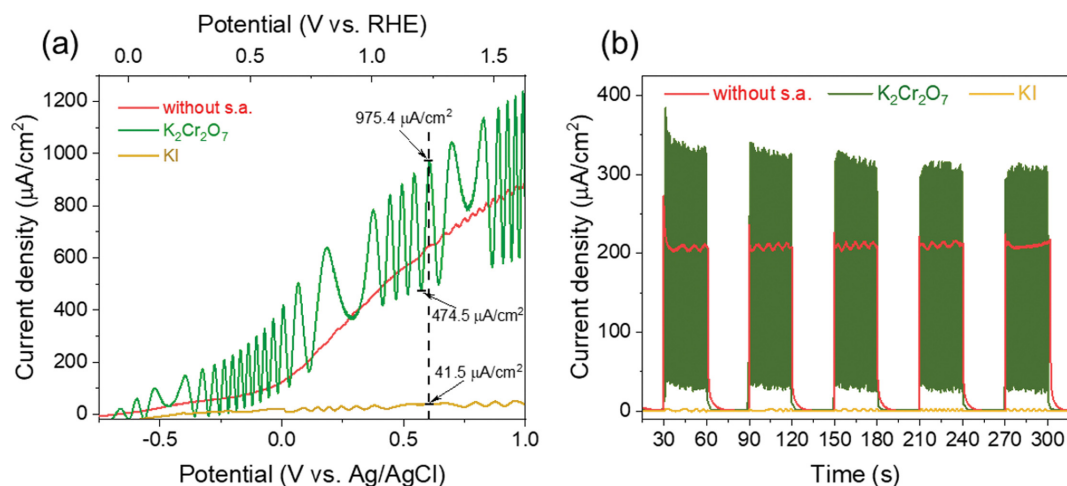


Fig. S2. LSV (a) and photoresponse ability (b) of  $\text{gC}_3\text{N}_4/\text{TNAs}$  without sacrificial agent and with  $\text{K}_2\text{Cr}_2\text{O}_7$  and KI as sacrificial agents.